High precision self-alignment using liquid surface tension for additively manufactured micro components

J. K. Overton[1], P. K. Kinnell*[2], S. D. A. Lawes[1], S. Ratchev[1]

[1]Manufacturing and Process Technologies Research Division, Department of M3, University of Nottingham, University Park, Nottingham, NG7 2RD, United Kingdom.

[2]Loughborough University, Wolfson School of Mechanical and Manufacturing Engineering, Loughborough, Leicestershire, LE11 3TU, United Kingdom.

**Corresponding Author. Tel.: (+44) 1509 227 146 Email address: p.kinnell@lboro.ac.uk*

Postal address: Loughborough University, Wolfson School of Mechanical and Manufacturing Engineering, Loughborough, Leicestershire, LE11 3TU, United Kingdom.

Abstract

Self-assembly of components using liquid surface tension is an attractive alternative to traditional robotic pick-and-place as it offers high assembly accuracy for coarse initial part placement. One of the key requirements of this method is the containment of the liquid within a designated binding site. This paper looks to expand the applications of self-assembly and investigates the use of topographical structures applied to 3D printed micro components for self-assembly using liquid surface tension. An analysis of the effect of edge geometry on liquid contact angle was conducted. A range of binding sites were produced with varying edge geometries, 45-135°, and for a variety of site shapes and sizes, 0.4 - 1 mm in diameter, and 0.5 x 0.5 – 1 x 1 mm square. Liquid water droplets were applied to the structures and contact angles measured. Significant increases in contact angle were observed, up to 158°, compared to 70° for droplets on planar surfaces, demonstrating the ability of these binding sites to successfully pin the triple contact line at the boundary. Three challenging self-assembly cases were examined, 1) linear initial component misplacement >0.5 mm, 2) angular misplacement of components, 3)

misplacement of droplet. Across all three assembly cases the lowest misalignments in final component position, as well as highest repeatability, were observed for structures with actual edge geometries <90° (excluding 45° nominal), where the mean magnitude of misalignment was found to be 31 μm with 14 μm standard deviation.

Keywords

Self-assembly, surface tension, micro assembly, micro parts, topographical, additive manufacturing, 3D printing

1. Introduction

Industrially manufactured products are typically assemblies made up of many separate and often dissimilar components. The assembly techniques required to realise these finished items are therefore of key importance to product generation. The micro component industry is rapidly growing and the continual trend of component miniaturisation has led to its own set of challenges that are not present in the macro domain. Simple pick-and-place operations become complex issues due to scaling effects, as parts become smaller gravity is no longer the dominant force. This is because surface forces scale with length, whereas gravity scales with length cubed [1]. This results in release problems due to adhesion forces between components and micro handling tools. Surface-related forces such as Van der Waals, electrostatic and surface tension dominate over gravitational force, which have led to novel handling strategies becoming the focus of much work. This includes the development of micro grippers [2-4], vacuum grippers [5], freeze grippers [6], as well as those based on electrostatic forces [7, 8].

An additional challenge for micro assembly in an industrial environment is that the process must be both fast and precise. Current methods make use of robotics to manipulate and place components; however these solutions either build assemblies with sub-micron accuracy at low speeds, or at high assembly speeds but with low accuracy [9]. There is also a cost trade-off to be made with faster more accurate systems being significantly more expensive. To lessen the

challenge of micro assembly an interesting concept is that of component self-assembly. Liquid self-assembly of components is an attractive alternative to traditional robotic pick-and-place techniques as it can offer very high final positional accuracy with fairly coarse initial placement. This means lower cost, faster pick-and-place systems, or the replacement of robotic pick and place with manual pick-and-place; leading to the advantages of either increased system flexibility, or reduced cost and higher throughput. The underlying concept behind liquid self-assembly is that features produced on the components can control droplet shape, and therefore surface tension, in such a way that the lowest energy state for the liquid is achieved when the components are well aligned. This principle is illustrated in Figure 1 which shows the droplet in place prior to assembly (a); followed by the drop wetting to both the static surface and the part (b). At this stage the non-symmetrical nature of the liquid surface results in surface tension forces that tend to move the part to a state of lowest surface energy; once the lowest surface energy state has been reached all surface tension forces are balanced (c).

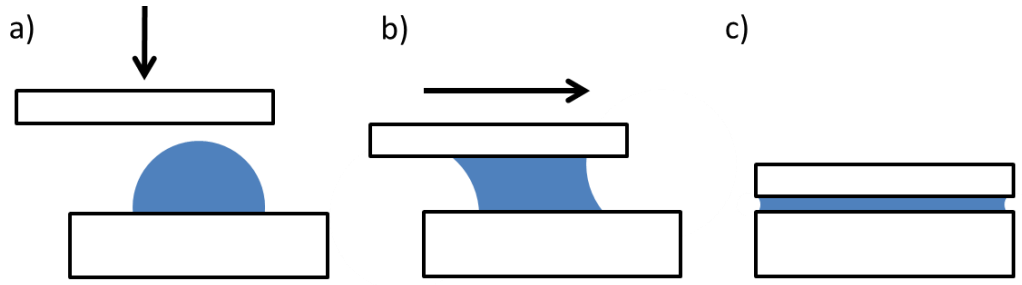

Figure 1: Self-alignment of component using liquid surface tension. a) Liquid droplet dispensed onto binding site and component moved into place, b) component comes into contact with liquid droplet and meniscus is formed, c) restoring forces act on component and it aligns to shape of binding site due to energy minimisation.

The controlled spreading of the assembly liquid is a key factor in this process, and much work has been carried out into this area. Several approaches have been developed in order to alter the wetting properties of specific regions of a surface. These include (super)hydrophilic and (super)hydrophobic target sites [10-15], (super)oleophilic and (super)oleophobic for oil-based liquids [16-18], micropillar arrays to create hydrophobic regions [19, 20], as well as most

recently, receptor sites with sharp edges to inhibit liquid spreading [21-24]. These methods can be divided into two distinct areas; those which rely on altering the surface properties of specific regions to influence wetting behaviour, and those that utilise physical geometric structures to constrain liquid spreading. Until now the majority of the literature in this field focuses on applications involving the use of microchips assembled on silicon wafers [25-28], with modifications to surface properties being introduced through a post-build process of coating, masking and etching. Typically this is achieved by thermally growing a silicon oxide layer on the wafer before a standard photolithography and reactive-ion etching (RIE) process is carried out to pattern the oxide layer [14, 21, 29] resulting in a hydrophilic surface. Other techniques [26, 27] also used black silicon coated with a fluoropolymer to realise a hydrophobic background material surrounding the binding sites.

As previously mentioned, one of the requirements of the self-assembly process is the confinement of the assembly liquid to a specified binding site. The ability to control liquid spreading through the use of sharp edges pinning the triple contact line (TCL) has been known for some time. The TCL is the equilibrium boundary where the solid-liquid-gas phases meet, with the shape of the liquid-gas interface determined by Young's equation:

$$0 = \gamma_{SG} - \gamma_{LS} - \gamma_{LG} cos\theta_c \qquad (1)$$

Where, γ_{SG} is the solid-gas interfacial energy, γ_{LS} is the liquid-solid interfacial energy, γ_{LG} the liquid-gas interfacial energy, and the equilibrium contact angle θ_c from the surface, as illustrated in Figure 2.

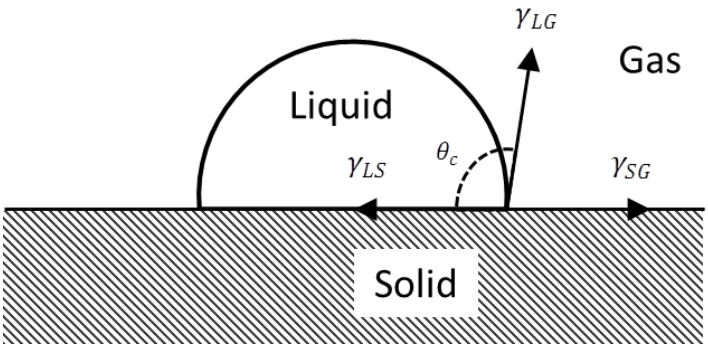

Figure 2: Diagram illustrating the quantities used in Young's equation (1).

Structures that control liquid spreading through halting the movement of the TCL at a defined edge are based on the mathematical inequality presented by Gibbs [30]:

$$\theta_c < \theta < (180° - \alpha) + \theta_c \qquad (2)$$

Where, θ is the contact angle of the droplet, θ_c is the Young's contact angle, and α is the angle of the sharp edge, see Figure 3.

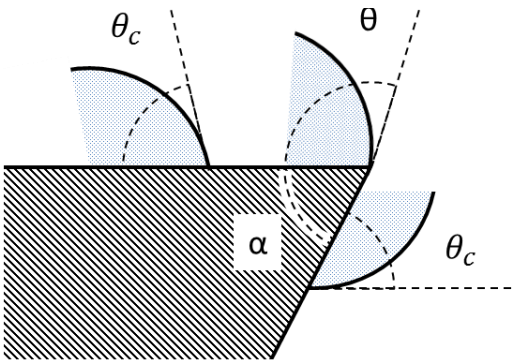

Figure 3: Spreading of a liquid droplet meeting a sharp edge as described by the Gibbs inequality, equation (2).

Overflow of the liquid assembly medium beyond the defined edge of the structure is catastrophic to self-assembly processes. Once the liquid is able to travel beyond the defined edge, the part to be assembled will be drawn along with the liquid, and out of alignment. It is therefore of critical importance to maximise the contact angle of the liquid when it is pinned at the boundary if robust self-assembly procedures are to be realised.

To extend the possible application of self-assembly to new areas this work will consider the relevance of the technique to additive manufacturing (AM) processes. The additive manufacturing industry offers many exciting possibilities for the rapid, flexible and cost-effective production of next generation products across a wide range of industrial sectors. The technology is typically used for modelling, prototyping, short-run production, and bespoke items, however as the process improves its use for final component manufacture is being seen. Examples of this can be seen in medical and dental implants, as well as technical applications such as the aerospace industry [31, 32]. Compared to traditional subtractive manufacturing methods AM offers much greater design flexibility with the realisation of intricate structures that cannot be manufactured using other methods, such as complex internal channels.

To our knowledge no work has been carried out to date on this manufacturing method for use in self-assembly applications using liquid surface tension. This work considers components in the 0.4 to 2 mm range, larger than typical micro assembly parts, as these are most immediately applicable to 3-dimensional assemblies whose major dimensions are in the z-axis. This includes assemblies such as micro-optical benches (MOB) [33, 34] and tactile probes for micro coordinate measuring machines (CMM) [35, 36]. This work builds on the current literature by presenting a detailed experimental analysis on the use of 3D printed topographical features for self-assembly using liquid surface tension. An analysis of the effect of the structure's edge geometry on the contact angle of the constrained liquid is presented for a range of different binding sites. Self-assembly of 3D printed components onto matching binding sites using liquid surface tension was investigated experimentally for three different alignment cases.

2. Liquid binding site optimisation

2.1. Methodology

The overall aim of this work was to examine the use of self-assembly using liquid surface tension to aid the assembly of 3D printed polymer components. This was assessed in two ways: The ability of topographical structures to prevent liquid spreading by measuring contact angles

of liquid droplets and the assembly of polymer components onto matching binding sites under three challenging assembly cases. The ability of topographical structures to control the spreading of liquid droplets by pinning the TCL was investigated by examining a range of simple structures. Circular binding sites from Ø0.4 – 1 mm and square binding sites 0.5 x 0.5 mm and 1 x 1 mm were manufactured with varying edge geometries. Edge geometries from 45 - 135°, in 15° increments were examined. Liquid water droplets were applied to the structures up to the point of collapse and their contact angles measured. Three different self-assembly cases were examined for 2 x 2 x 0.5 mm rectangular prism components assembled onto matching binding sites, with edge geometries from 45 - 135° in 15° increments.

Full details of the fabrication process used to create the test structures, as well as the experimental details are presented in the subsequent sections.

2.2. Fabrication

Components were manufactured using projection-micro-stereolithography (PMSL), a solid free-form fabrication technique based on controlled solidification of a liquid, light-sensitive resin when exposed to a light source (photopolymerisation). Using an LCD or Digital Micromirror Device (DMD) the polymer is successively exposed and solidified in 25 µm layers to construct 3D geometries according to data from an STL file. An EnvisionTec Perfactory Mini-Multi lens projection stereolithography machine using EnvisionTec R11 rapid prototyping material was used. This resin was chosen due to its well established curing behaviour in the build process. Projector brightness was calibrated to 600 mW/dm^2 with exposure time of 4.0 seconds/layer (standard range), at a layer height of 25 µm. Resolution was set to 1050 x 1400 pixels equivalent to a pixel size of 5 µm in X.Y-direction.

2.3 Test geometries

Structures were designed to examine the effect of edge geometry on the ability to pin the TCL of a spreading liquid droplet. Since droplets have a spherical shape when in their lowest energy state circular binding sites were selected. This was also due to their axial-symmetry and ease of

manufacture. Components containing test arrays of Ø0.4, 0.5, 0.6, 0.75 and 1 mm circular binding sites were manufactured in the aforementioned method (see Figure 4). Test arrays containing square binding sites of 0.5 x 0.5 mm and 1 x 1 mm were manufactured using the same method. Each feature was located in a 0.1 mm deep hole, while being 0.1 mm tall, resulting in the binding site surface being flush with the surface of the bulk material of the test array. Due to the absorption of light, the minimum achievable layer thickness was 25 μm. For practical applications it is desirable for the binding site to have a shallow profile. A binding site height of 100 μm was considered suitable for producing the range of edge geometries while limiting layer numbers and therefore reducing the likelihood of production defects occurring. This corresponded to a binding site height of 4 build layers. The diameter of the "trench" surrounding each structure was Ø1.5 mm for circular binding sites, and 2 x 2 mm for square binding sites. This design was chosen in order to protect the edge of the binding sites from damage during the handling and cleaning process and to give sufficient clearance between the structures and surrounding bulk material to prevent any interaction when applying the liquid. A cross-sectional example of the binding site geometry used for this work can be seen in Figure 5.

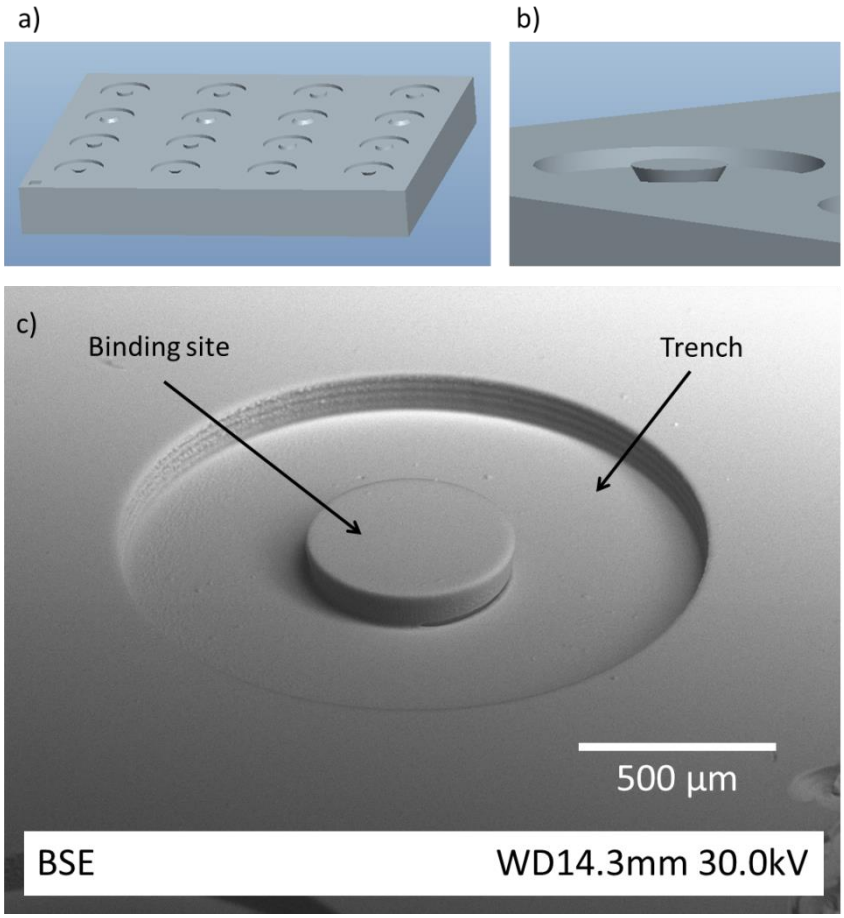

Figure 4: a) Rendered image of test component with array of Ø0.5 mm circular binding sites, b) Rendered image of a single binding site with 45°nominal edge geometry, c) SEM image of Ø0.6 mm circular binding site with 60° nominal edge geometry.

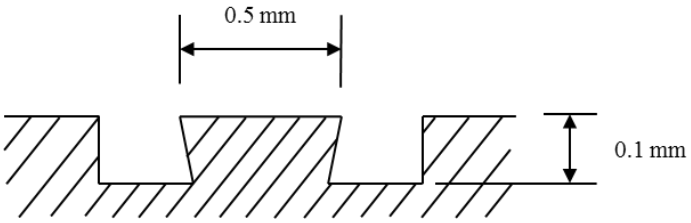

Figure 5: Cross-sectional diagram of binding site geometry for Ø0.5 mm circular binding site.

The structures' sharp edges were altered to investigate acute (undercut) angles, and obtuse (chamfer) angles, as seen below in Figure 6. Edge geometries of 45-135° were manufactured for all above mentioned structures in 15° increments. Additional angles of 85 and 95° were manufactured for Ø0.5 and 1 mm circular binding sites as the area around 90° was believed to

be a key angle of interest. All binding sites were inspected after manufacture under an optical microscope before carrying out further experiments.

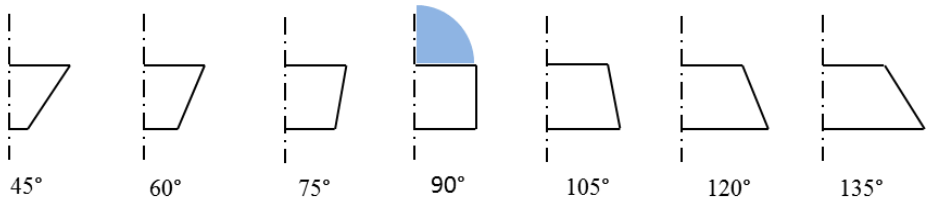

Figure 6: Nominal edge geometries of topographical structures. Blue region indicates liquid droplet placed on top surface of the structure.

2.4. Experimental setup

Experiments were conducted in an air-conditioned laboratory environment at 20° Celsius. All components were manufactured in a temperature controlled lab at 21° Celsius. Before testing parts were cleaned in an ultrasonic isopropanol alcohol bath for 3 minutes, followed by a second isopropanol solution for a further 3 minutes, and allowed to dry in air. Components were mounted on an X-Y precision stage and viewed under an optical microscope with a JVC TK-C1381 CCD mounted camera. Data were captured using a Hauppage Win-TV-HVR-1900 interface with post process image analysis conducted using the ImageJ software package. Contact angles were analysed using the public domain Low bond axisymmetric drop shape analysis (LB-ADSA) plugin, developed by A. Stalder [37]. Liquid water droplets were applied to the target sites using a digital timed precision fluid dispenser TS-250 from Adhesive Dispensing Ltd. A 3cc syringe barrel was used in conjunction with a 34 gauge blunt end dispending tip. The liquid used for the experiments was water with surface tension, γ=72.9 mN m^{-1}. Droplets were dispensed onto the centre of the binding sites incrementally to increase the volume of the droplet. After each application the droplet was allowed to stabilise and reach equilibrium before proceeding with further applications. Droplets were applied up to the point of collapse when the liquid escaped the binding site and was no longer constrained. The liquid was then removed from the surface using a dry compressed inert gas. Each binding site was

manufactured twice, and the experiment was conducted 5 times for each site, resulting in 10 data points (N=10).

Self-assembly tasks were performed by applying a single liquid water droplet to the binding site. Components were manipulated by hand using tweezers and brought into contact with the liquid droplet before release. Components were allowed to reach their equilibrium position which was then analysed post-experiment by measuring the difference between component and binding site centres using ImageJ software.

Scanning Electron Microscope images were captured using a Hitachi S-2600N SEM operating in low vacuum mode at 30kV acceleration voltage.

3. Constraint of liquid spreading using topographical structures

A flat plain substrate was manufactured using the fabrication method described in 2.2. Water was dispensed onto the plain substrate and the natural contact angle of water was measured to be 70°. Water was then applied to the test structures in turn using the equipment and method outlined in 2.4. Optical microscope images illustrating the difference between the natural contact angle on the plain substrate and an isometric view for an undercut binding site can be seen in Figure 7, illustrating the dramatic effect that is made possible with the undercut binding sites.

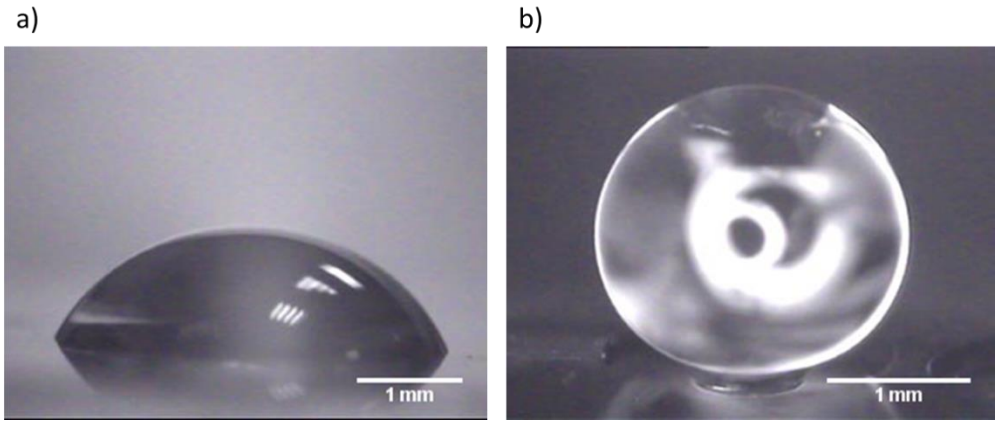

Figure 7: Optical microscope images of water droplets; a) unconstrained droplet on plain substrate, b) isometric view of droplet constrained to Ø1 mm circular binding site with 60° nominal edge geometry.

The results collected for the maximum contact angle before droplet collapse are shown in Figure 8, plotted against nominal edge geometry. Each data point represents an average of 10 measurements. From these data it can be seen that higher contact angles were achieved for the Ø0.5 mm binding site compared to the Ø1 mm site. There are a number of reasons that could explain this result: firstly by doubling the diameter of the binding site the surface area is increased by a factor of 4. This would mean that a significantly greater volume of liquid is being applied to the binding site. When the droplet is small enough gravitational effects will be negligible but as the diameter approaches a certain length, known as the capillary length (equation (3)), they will start to play a role once again. For water at atmospheric pressure and 20° Celsius: γ = 72.9 mN m^{-1}, ρ = 998.21 kg m^{-3}, g = 9.81 ms^{-2}, giving a capillary length of 2.7 mm.

$$\lambda_c = \sqrt{\frac{\gamma}{\rho g}} \qquad (3)$$

Where, g is acceleration due to gravity, ρ is fluid density and γ is surface tension. The average measurement of the droplet diameter for the binding site achieving the highest contact angle on the Ø0.5 mm binding site was 1.32 mm, whereas for the Ø1 mm site an average diameter of 2.12 mm was measured. This shows that for the larger diameter binding site the droplet diameter had started to approach the capillary length, leading to gravitational effects acting on

the droplet with proportionally greater effect. It is therefore proposed that this could have the effect of making the droplet unstable, causing it to collapse at lower contact angles.

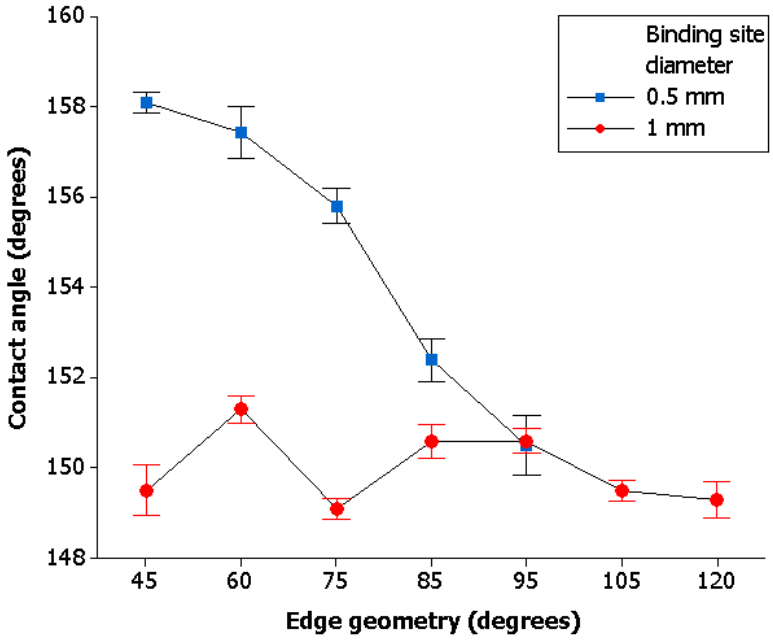

Figure 8: Contact angle of water droplets on circular binding sites for full range of nominal edge geometries. Error bars display standard deviation.

Other factors that could influence a lower contact angle are also any defects that occur at the edge of the geometry. As the diameter of the structure increases, so too does its perimeter, and with a greater perimeter length the likelihood of manufacturing defects along the length of this critical feature increases. Preventing liquid spreading with a topographical edge relies on the integrity of the structure. Once the droplet begins to slide down the vertical face of the structure failure is uncontrollable and catastrophic, leading to droplet collapse and spreading outside of the designated binding site. Contact angles can be seen to decrease rapidly for Ø0.5 mm binding sites once the edge geometry becomes larger than 75°. It should be noted that no data was plotted for 105 -135° for Ø0.5 mm, and also 135° for Ø1 mm. This was due to the fact that as the angle increased above 105° the binding sites were not able to support the liquid droplets with good stability. As a result the droplet would slide down the vertical face almost immediately, becoming pinned once the bottom of the slope had been reached. Although the

droplet did not immediately collapse, the fact that it was no longer constrained to the binding site was deemed unacceptable as this would cause systematic misalignment. Based on the initial findings, only edge geometries from 45-90° were examined for the remainder of the binding site diameters. Data presented in Figure 9 show fairly close grouping as there is only a difference in contact angle of 9° across all binding sites. Points of interest from this graph are the low contact angle measured for Ø0.6 mm x 45°, and the missing data point for Ø0.4 mm x 45°.

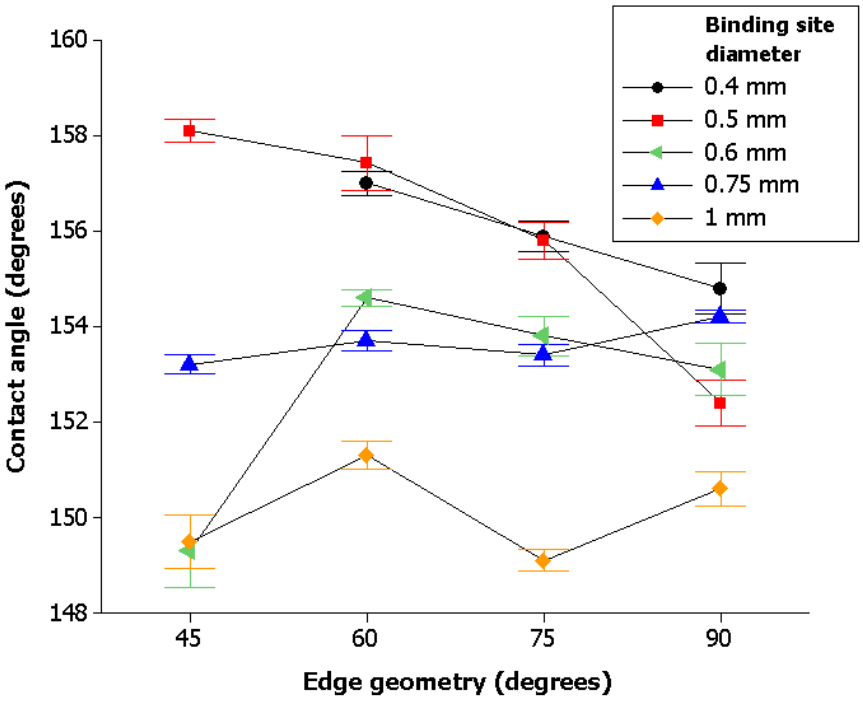

Figure 9: Contact angle of water droplets on circular binding sites for different nominal edge geometries. Error bars display standard deviation.

Subsequent SEM analysis of these binding sites revealed that these particular structures were either damaged in the manufacturing process or failed to build correctly based on their geometry. Figure 10 a) and b) show Ø0.4 mm binding sites, and c) and d) show Ø0.6 mm binding sites. Both images a) and c) appear to have a jagged edge which would indicate a brittle failure caused by mechanical damage to the structures. Image d) appears to be smoother and would point towards a defect in the build process. The top surface of the structure in image b)

can be seen to be curling upwards which would suggest a contraction of the resin due to evaporation. This has led to the development of cracks in the structure which are indicated in the image by white arrows. It is worth noting that none of these manufactured structures displayed a 45° edge geometry and would imply that this level of negative incline (1:1) may not be suitable for the manufacturing method. However, it can be seen from Figure 8 and Figure 9 that for binding sites with a diameter of 0.5 mm or less there is a practical benefit to using edge geometries below 90°.

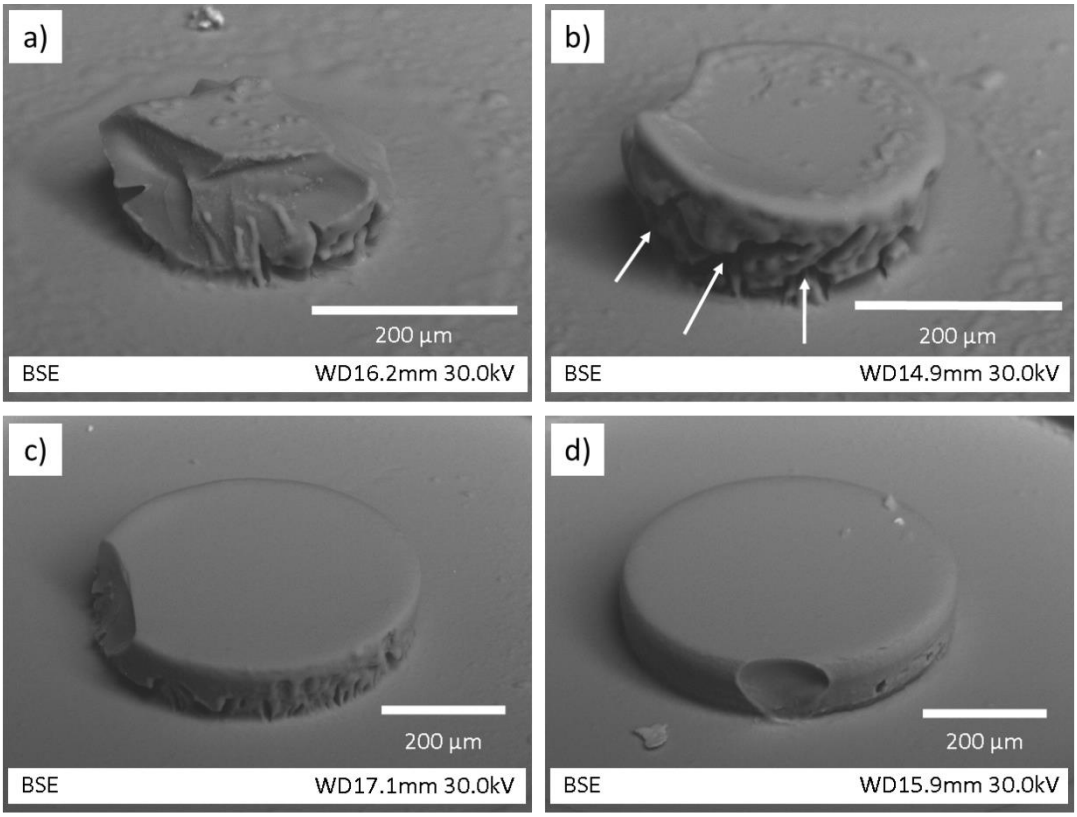

Figure 10: SEM images showing defects present on circular binding sites; a) and b) show Ø0.4 mm x 45° edge geometry, c) and d) show Ø0.6 mm x 45° edge geometry. White arrows indicate cracks in the structure caused by contraction due to evaporation in the curing process.

Typically for a self-assembly process the binding site shape will match that of the component. In order to achieve both axial and rotational alignment a square shape will be necessary. 0.5 x 0.5 mm and 1 x 1 mm square binding sites were manufactured and examined using the same fabrication and testing procedure. From the results presented in Figure 11 it can be seen that the

resulting contact angles are similar to those seen for the circular sites, showing a shallower contact angle with increasing site size and steeper contact angle as the angle of the edge geometry decreases. The 1 x 1 mm binding site has a lower contact angle overall which is believed to be caused by the previously discussed effects of droplet diameter approaching the capillary length, and larger structures have more frequent occurrence of edge defects from manufacturing.

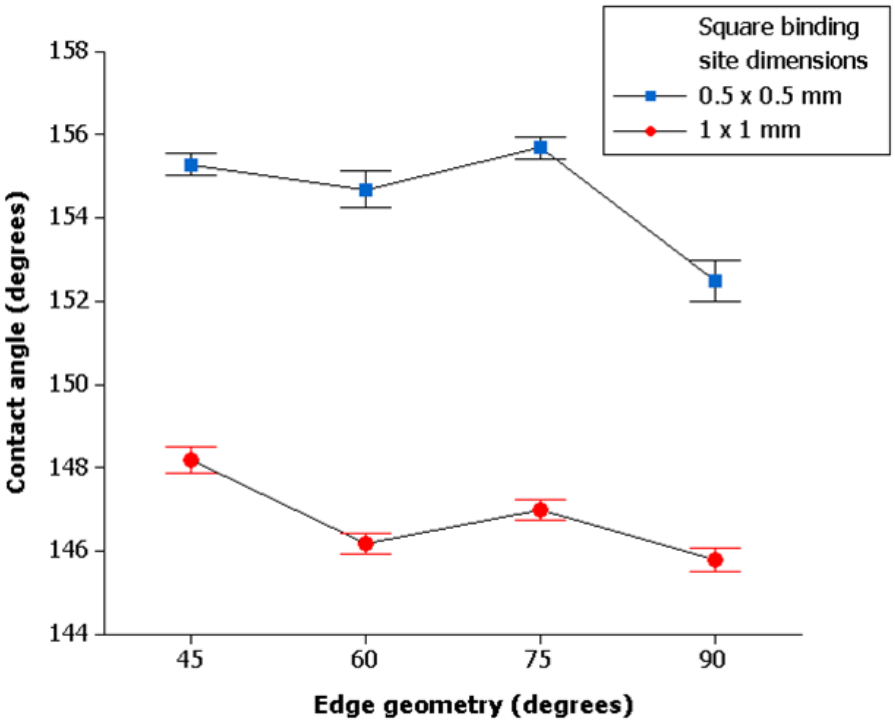

Figure 11: Contact angle of water droplets on square binding sites for different nominal edge geometries. Error bars display standard deviation.

Given the results observed for circular, 0.5 x 0.5, and 1 x 1 mm square binding sites, it was clear that the produced edge geometries may not match the nominal; designed geometries. In order to better understand how effective the production process was at achieving the nominal edge geometries square binding sites of 2 x 2 mm surrounded by 3 x 3 mm trenches were designed for the following experiments so they could be easily cross-sectioned and examined.

4. Cross-sectional analysis of structures

In order to assess the manufacturing processes ability to realise the desired edge geometries, square binding sites of 2 x 2 mm surrounded by 3 x 3 mm trenches were manufactured using the process outlined in section 2.2. Binding site cross sections were examined by optical microscopy following a series of manual grinding operations on P400 to P4000 SiC paper. The cross section perpendicularity was ensured by means of a parallel bar. Examples of four binding sites can be seen below in Figure 12 which shows images of actual edge geometry angles for the four nominal angles of 60°, 90°, 105°, and 135°.

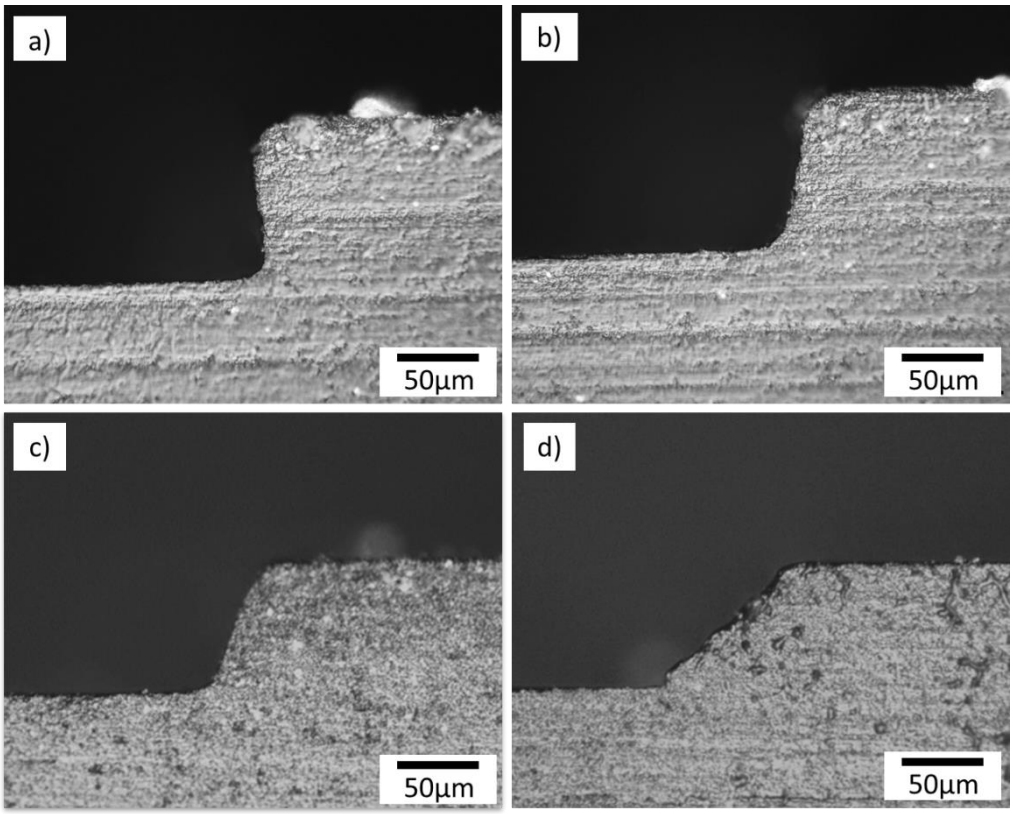

Figure 12: Optical microscope images of cross-sectioned binding sites. a) 60° nominal, b) 90° nominal, c) 105° nominal, and d) 135° nominal.

The average actual edge geometry is presented below in Table 1 against the nominal angle, along with the standard deviation. From the data it can be seen that the manufacturing process struggles to recreate the nominal angles faithfully, with angles being greater than desired. This is more pronounced for angles <90° whereby the average measured angles were all close to

~85° regardless of the intended nominal angle. The large standard deviation observed for 45° nominal shows a high variability in the angles produced and correlates with the inconsistent results observed in section 3.

Nominal edge geometry (degrees)	Average actual edge geometry (degrees)	Standard deviation
45	83	8.9
60	85	5.2
75	86	2.5
90	99	4.8
105	117	5.4
120	123	1.4
135	136	1.4

Table 1: Table summarising the average actual edge geometry compared to the nominal value.

5. Self-assembly of components using liquid surface tension

To study the capability of these sites to align parts by liquid surface tension a series of experiments were conducted where test components were placed onto the wetted sites with a large initial misalignment. The geometry of the sites was varied, and three distinct initial conditions were investigated, so that the ability to align both position and orientation could be considered. Square structures of 2 x 2 mm surrounded by 3 x 3 mm trenches, were manufactured using the previously defined technique and nominal edge geometries from 45-135° were examined. The components used in the assembly tasks were rectangular prisms whose square bases matched those of the top surface of the binding sites, with dimensions 2 x 2 x 0.5 mm. Components were manufactured using the same material and fabrication techniques as the binding sites, detailed in section 2.2. Components were examined under an optical microscope and dimensions were within the expected 5% shrinkage inherent to the manufacturing process. All component dimensions referred to in this paper are nominal. A single liquid water droplet was applied to the surface of the topographical structure and the component then placed by hand using tweezers. No special placement devices were used and as such the test represents a robust analysis of a challenging alignment task. To establish the variability of the human operator at depositing liquid to the binding sites, a random sample of 10 assembly cases were analysed whereby the average liquid volume was determined to be 128 nl with a standard deviation of 11 nl. The magnitudes of the combined misalignment in both x

and y axis for droplet placement relative to the centre of the binding site was 216 µm with a standard deviation of 53 µm.

The three assembly cases examined in this work are shown below in Figure 13: a) x-offset, where the component was offset from the target position by 500 µm along the x-axis (25% of the binding site dimension); b) twist-offset, where the component was positioned over the centre of the binding site, but rotated by 35° about the z-axis; and finally c) droplet-misalignment, where the liquid droplet was placed in the corner of the binding site and the component released directly over the droplet. For all cases we were interested in the linear alignment capabilities of the structures when components were subjected to large initial misalignments. All assembly cases were carried out across the full range of edge geometries and repeated ten times each (N=10). This information is summarised below in Table 2.

Once more, a random sample of 10 results was examined for each assembly case to assess the repeatability of component release position. For *case a)* the average x-offset was 574 µm with a standard deviation of 29 µm. For assembly *case b)* the average angle of release was 35.3°, standard deviation 1.3°. Repeatability of *case c)* was determined by calculating the magnitude of offset in both x and y axes between the component and binding site centres. This was found to be 691 µm with standard deviation of 90 µm.

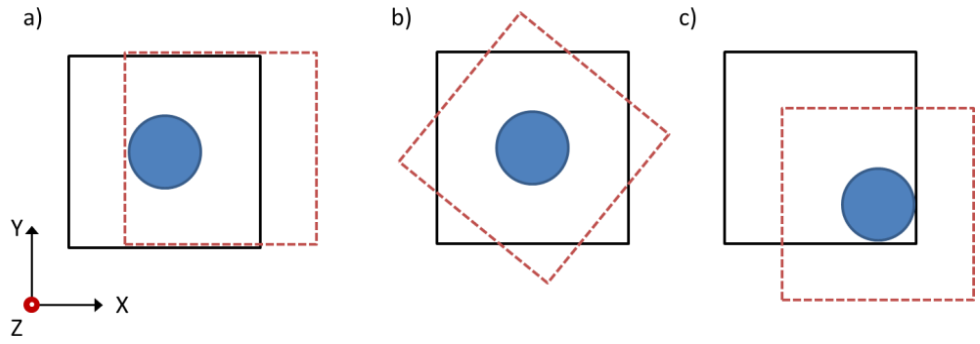

Figure 13: Schematic showing the three assembly cases examined in this work. Dotted line represents release position for component: a) x-offset, b) twist-offset, and c) droplet misalignment.

Case	Edge geometry (degrees)	Nominal component offset	Actual component offset	Standard deviation
a)	45 [83], 60 [85], 75 [86], 90 [99], 105 [117], 120 [123], 135 [136]	500 µm	574 µm	29 µm
b)	45 [83], 60 [85], 75 [86], 90 [99], 105 [117], 120 [123], 135 [136]	35°	35.3°	1.3°
c)	45 [83], 60 [85], 75 [86], 90 [99], 105 [117], 120 [123], 135 [136]	-	691 µm	90 µm

Table 2: Summary of self-assembly tests carried out. Edge geometry represents actual angle, with corresponding nominal angle shown in square brackets.

The assembly process was recorded using the aforementioned acquisition techniques. Final assembly misalignment of the components was analysed using ImageJ software, with an x-y coordinate recorded for the difference between the component and binding site centres. To determine the precision of the measurement system, a known component was measured 20 times and the repeatability of the system was determined to be 3 µm.

Coordinate data for *case a)* x-offset, are displayed in the scatter plot, and the combined magnitudes of the misalignments in x and y axes in the boxplot in Figure 14 a) and b) respectively. From the data it can be seen that the magnitude of misalignment is significantly higher for edge geometries greater than 100°, with the data also being more spread. This indicates that the assembly process is a lot less reliable than for binding sites which have edge geometries of 100° or less. Rather than consider the data presented in figure 14 as a whole it is convenient to consider the binding sites for their capability to achieve particular tolerances of assembled precision. Two threshold values have been selected, 25 µm and 100 µm of precision, and the effectiveness of the binding sites were evaluated against these thresholds, results shown in figure 15.

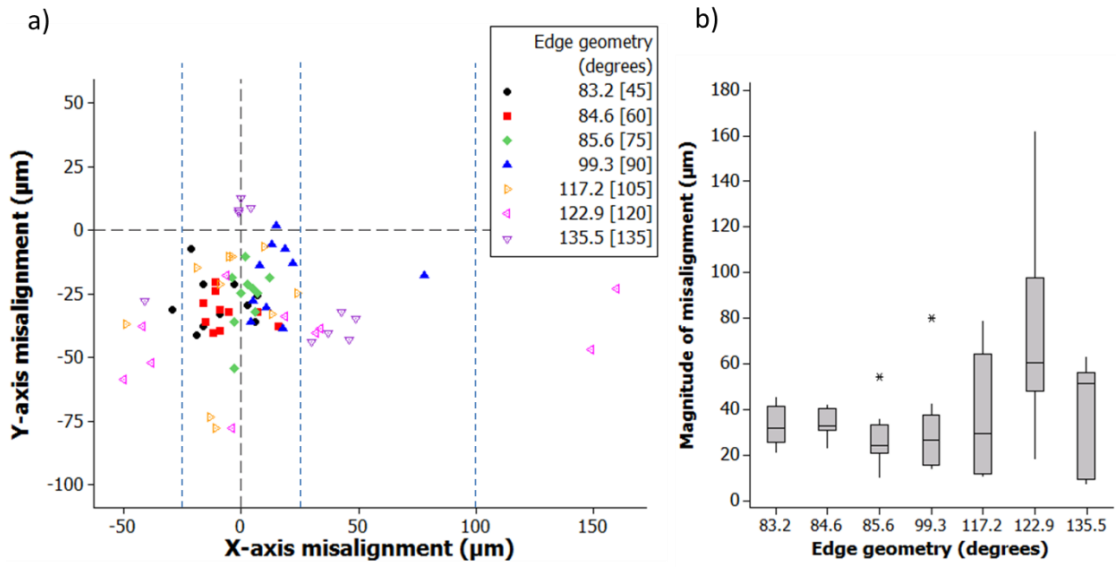

Figure 14: Assembly results for x-offset tests: a) scatter plot and b) box plot. Dotted lines indicate threshold regions of 25and 100 µm misalignment in the x-axis. Numbers in square brackets represent the nominal edge geometries. Asterisks indicate outliers in the data.

For *case a)* the threshold was applied to the x-axis only, and to both x and y-axes for *cases b)* and *case c)*. From Figure 15 it can be seen that the greatest capacity for alignment was realised for structures with an actual edge geometry <100°. The structures with 45° nominal edge geometries are an exception however, with lower success rates observed at both thresholds across the three assembly cases. This is believed to be due to the high variability in the actual manufactured angle which can be seen by the high standard deviation in Table 1. For structures with actual edge geometries greater than 100° the success rate is much lower and the assembly procedure becomes less reliable. Even though the success rate is still fairly high in *case a)*, looking at the box plot in Figure 14 b) it can be seen that the magnitudes of the misalignments are much higher as well as the standard deviation of data. Sites with actual edge geometries >100° do however show the capability to provide alignment when considered against the threshold criteria, see figure 15.

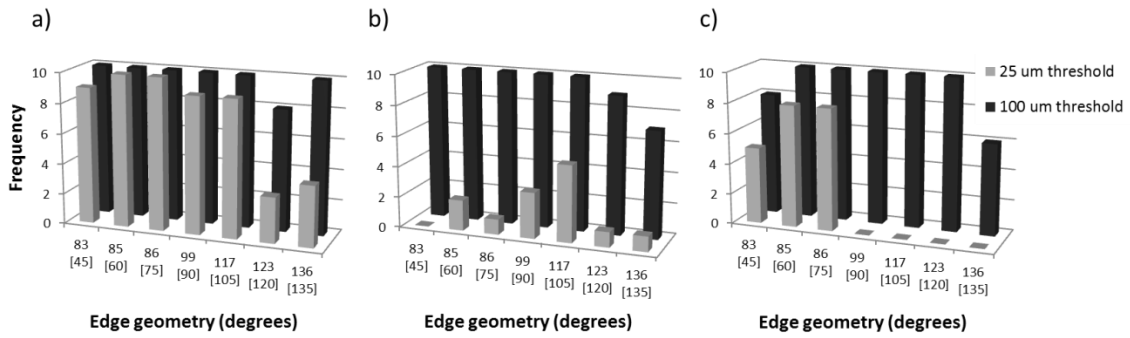

Figure 15: Bar charts showing component assembly success rates for misalignments less than or equal to the given threshold in both x and y axis: a) x-offset, b) twist-offset, c) droplet misalignment. X-axis displays the measured edge geometry, with corresponding nominal angle shown in square brackets.

For sites with edge geometries >100° there is significant standard deviation in the final misalignment. This makes the interpretation of this data very difficult, which is an aspect not captured by the threshold plots. It was decided to exclude this data from further analysis and focus on structures with actual edge geometries below 100°, i.e. nominal angles of 45°, 60°, 75° and 90°, where similar trends might be observed but with less significant standard deviation.

Although this study was primarily interested in linear alignment capabilities, it was observed that all components aligned within ~2° about the z-axis, even when under extreme rotational misalignment in *case b)*. The only exception to this was the components that failed to align altogether, and these were the cases that fell outside the 100 μm threshold. The findings presented in this section are in agreement with the results in section 3 which showed a significant reduction in contact angle achieved when the edge geometry was increased beyond 90°. Comparison of the initial contact angle measurements and the alignment experiments would suggest that the liquid contact angle observed for isolated droplets is a useful indicator of performance in alignment tasks.

Excluding the data outside the 100 μm misalignment threshold, an analysis of the spread of successful assembly cases can be observed. From the data (Figure 15 and Figure 16) it can be seen that structures with an edge geometry less than 90° (excluding 45° nominal) have the most

consistent set of results having a combined success rate of 96.7%, and a fairly even spread of data across the three different assembly cases. For structures having a 45° and 90° nominal edge geometry the misalignment magnitudes are similar to those for <90°. However the failure rate is higher meaning the data set is therefore smaller and less reliable. The mean misalignment for angles >90° in *case c)* is much greater, as is the range of results. Based on the box plot in Figure 15 c), it can be seen that there were no successful assembly cases at the 25 µm threshold for structures with edge geometries >90°. This indicates the poor alignment capability of the >90° edge geometries when the assembly task becomes more challenging.

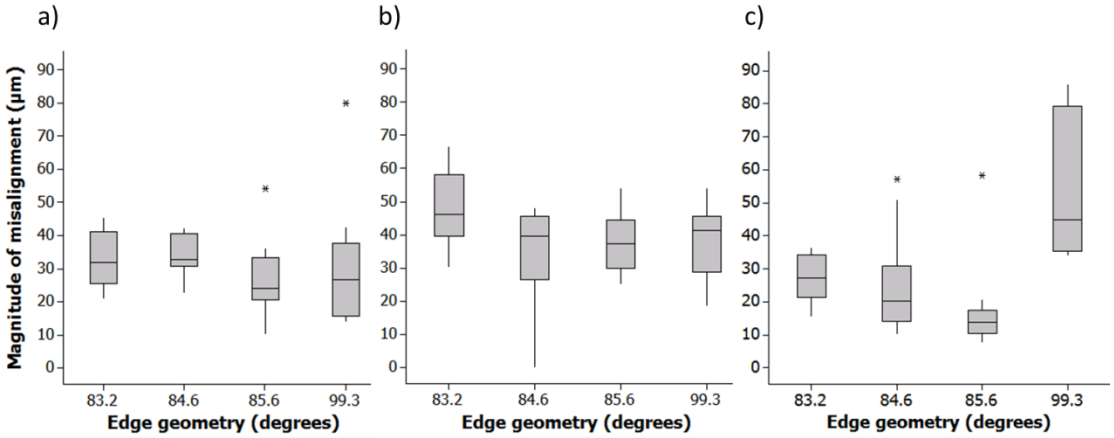

Figure 16: Boxplots of assembly results showing magnitude of component misalignment in both x and y axis against binding site edge geometry for assembly cases falling within the ±100 µm threshold: a) x-offset, b) twist-offset, c) droplet misalignment. Asterisks indicate outliers in the data.

In order to better understand this variation in performance scanning electron microscopy (SEM) was performed to investigate the binding sites. This revealed that defects had been introduced in the fabrication of the structures with 45° nominal edge geometries. Figure 17 a) shows the correctly fabricated structure, however the opposite edge of the same binding site, displayed in Figure 17 b) shows that the structure has not formed correctly and material has gathered to form a radius.

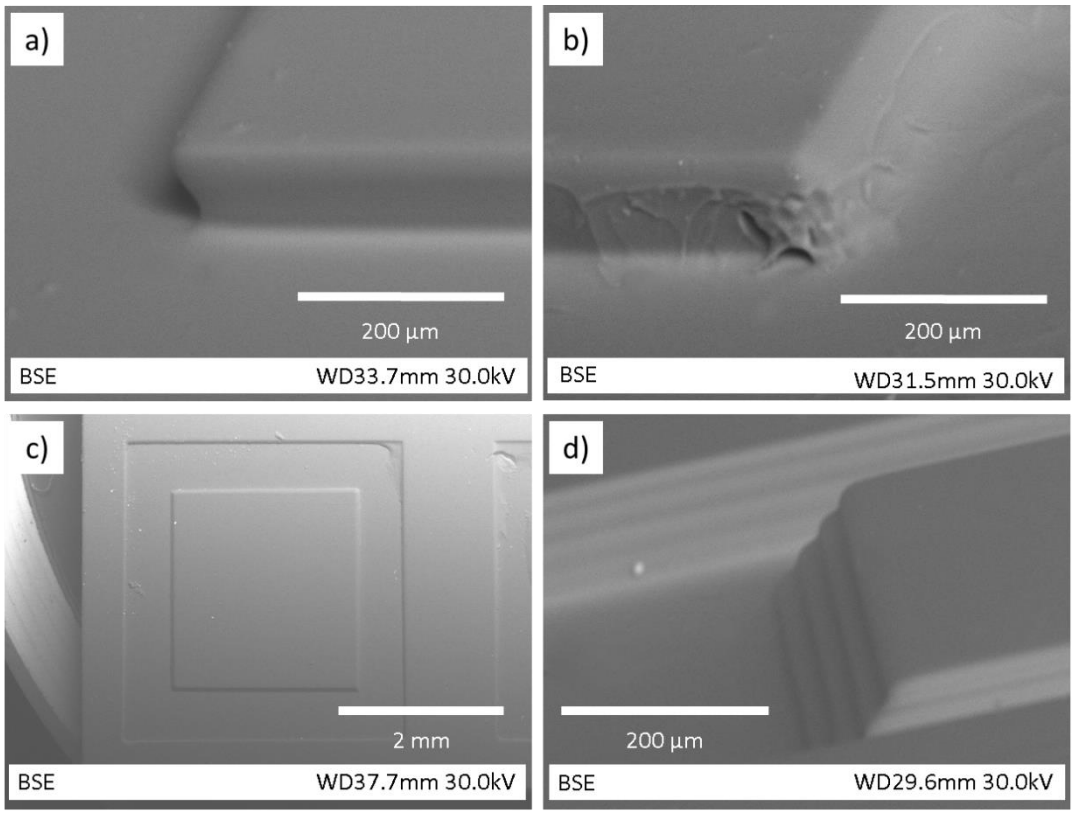

Figure 17: SEM images of 2 x 2 mm assembly structures. a) 45° nominal edge geometry, b) 45° nominal with incorrectly manufactured edge geometry, c) top-down view of 105° structure, d) 135° structure clearly showing stepping of individual 25 µm layers.

These defects could explain the failed assembly attempts observed for the 45° nominal edge geometries and is in agreement with the high standard deviation observed with the cross-sectional analysis in section 4. Figure 17 d) illustrates the defects in the sites produced with edge geometries >90° The individual 25 µm layers can clearly be seen to have produced step features, and that a smooth incline was not achieved. From the images obtained it would appear that each layer was effectively only a straight 90° edge offering no benefit going beyond a complete 90° edge geometry. Experimental observations found that during assembly the liquid would meet the edge of the binding site and overflow, proceeding to the next edge on the 25 µm layer below, and so on. It was seen that when the liquid had overflown, the component would align to the geometry of the lower layers. This would explain the consistently high

misalignments observed, and the large number of cases falling outside of the assembly thresholds.

This work has shown that even without a well-defined sharp edge, accurate and repeatable assembly of micro components using liquid surface tension is achievable. Across all three assembly cases components were assembled onto binding sites with actual edge geometries <90° (excluding 45° nominal), with an average misalignment magnitude of 31μm and 14 μm standard deviation.

6. Conclusions

This work has demonstrated that component alignment relies on careful constraint of droplet position and shape. Droplet shape on circular binding sites with varying degrees of edge geometry was investigated and significant increases in contact angle of liquid water droplets were observed, with contact angles up to 158° achieved compared to 70° on the plain substrate. This suggests that edge geometry has a dramatic effect on the ability to pin the TCL. A decrease in the contact angle was observed for structures where the nominal edge geometry was greater than 90°, compared to angles achieved for structures with nominal edge geometries less than 90°, implying that >90° offer significantly less constraint.

Cross-sectional analysis revealed that the manufacturing process failed to produce the nominal angles, with actual edge geometries closer to 90°. SEM imaging showed a distinct stepping of the individual layers for structures with actual edge geometries >100° which compromised the self-alignment process, as the droplet was able to overflow the top layer of the binding site. Once the droplet had spread beyond the binding site the assembly process was not recoverable, with the component drawn along with the spreading droplet leading to large misalignments. An investigation of the effect of individual layers on the ability to pin the TCL is therefore recommended as the subject for future work.

Despite the discrepancy between nominal and actual edge geometries all structures displayed a capacity for alignment at the 100 μm threshold for the three assembly cases. Clear benefits were observed for structures with actual edge geometries <90° (excluding 45° nominal) which achieved repeatable alignment at the 25 μm threshold, with a mean misalignment of 31 μm and 14 μm standard deviation.

While the work presented in this paper focuses on structures created using PMSL, it is believed that this technique could be applied to other additive manufacturing processes, as well as subtractive manufacturing processes such as micro milling, and micro electro discharge machining.

This work has demonstrated that the self-assembly processes is tolerant of defects on the binding site, and that without a well-defined sharp edge, accurate and repeatable self-assembly under challenging assembly conditions is achievable by undercutting the topographical structure.

Acknowledgements

The authors would like to acknowledge the generous funding provided by the Engineering and Physical Sciences Research Council EPSRC that has made this research possible.

Authors would like to thank the Manufacturing and Process Technologies Research Division at the University of Nottingham for the use of state of the art equipment that enabled this work to be carried out.

References

[1] Mastrangeli M, Abbasi S, Varel C, Hoof CV, Celis JP, Böhringer KF. Self-assembly from milli- to nanoscales: methods and applications. Journal of Micromechanics and Microengineering. 2009;19:083001.

[2] Rakotondrabe M, Ivan IA. Development and force/position control of a new hybrid thermo-piezoelectric microgripper dedicated to micromanipulation tasks. IEEE Transactions on Automation Science and Engineering. 2011;8:824-34.

[3] Chen BK, Zhang Y, Sun Y. Active release of microobjects using MEMS microgripper to overcome adhesion forces. JOURNAL OF MICROELECTROMECHANICAL SYSTEMS. 2009;18:652-9.

[4] Imai S, Ishikawa T, Sato M, Sato H, Tamura K. Handling Characteristics of Mems-Tweezers with Contact Surface Fabricated by Deep-Rie. Journal of Advanced Mechanical Design, Systems, and Manufacturing. 2010;4:150-7.

[5] Bos EJC, Bullema JE, Delbressine FLM, Schellekens PHJ, Dietzel A. A lightweight suction gripper for micro assembly. Precision Engineering. 2008;32:100-5.

[6] López-Walle B, Gauthier M, Chaillet N. Dynamic modelling for a submerged freeze microgripper using thermal networks. Journal of Micromechanics and Microengineering. 2010;20:025001.

[7] Dalin J, Wilde J, Zulfiqar A, Lazarou P, Synodinos A, Aspragathos N. Electrostatic attraction and surface-tension-driven forces for accurate self-assembly of microparts. Microelectronic Engineering. 2010;87:159-62.

[8] Hesselbach J, Wrege J, Raatz A. Micro Handling Devices Supported by Electrostatic Forces. CIRP Annals - Manufacturing Technology. 2007;56:45-8.

[9] Berthier J, Brakke K. The Physics of Microdroplets: John Wiley & Sons, 2012.

[10] Sato K. Self-alignment of microparts using liquid surface tension-behaviour of micropart and alignment characteristics. Precision Engineering. 2003;27:42-50.

[11] Fantoni G, Hansen HN, Santochi M. A new capillary gripper for mini and micro parts. CIRP Annals - Manufacturing Technology. 2013;62:17-20.

[12] Li X-M, Reinhoudt D, Crego-Calama M. What do we need for a superhydrophobic surface? A review on the recent progress in the preparation of superhydrophobic surfaces. Chemical Society Reviews. 2007;36:1350-68.

[13] Feng L, Li S, Li Y, Li H, Zhang L, Zhai J, et al. Super-Hydrophobic Surfaces: From Natural to Artificial. Advanced Materials. 2002;14:1857-60.

[14] Fukushima T, Iwata E, Ohara Y, Murugesan M, Bea J, Lee K, et al. Multichip Self-Assembly Technology for Advanced Die-to-Wafer 3-D Integration to Precisely Align Known Good Dies in Batch Processing. Components, Packaging and Manufacturing Technology, IEEE Transactions on. 2011;1:1873-84.

[15] Chang B, Shah A, Routa I, Lipsanen H, Zhou Q. Surface-tension driven self-assembly of microchips on hydrophobic receptor sites with water using forced wetting. Applied Physics Letters. 2012;101:114105.

[16] Bo C, Sariola V, Aura S, Ras RHA, Klonner M, Lipsanen H, et al. Capillary-driven self-assembly of microchips on oleophilic/oleophobic patterned surface using adhesive droplet in ambient air. Applied Physics Letters. 2011;99:034104--3.

[17] Feng L, Zhang Z, Mai Z, Ma Y, Liu B, Jiang L, et al. A Super-Hydrophobic and Super-Oleophilic Coating Mesh Film for the Separation of Oil and Water. Angewandte Chemie International Edition. 2004;43:2012-4.

[18] Tuteja A, Choi W, Ma M, Mabry JM, Mazzella SA, Rutledge GC, et al. Designing Superoleophobic Surfaces. Science. 2007;318:1618-22.

[19] Yeo J, Choi MJ, Kim DS. Robust hydrophobic surfaces with various micropillar arrays. Journal of Micromechanics and Microengineering. 2010;20:025028.

[20] Shao J, Ding Y, Wang W, Mei X, Zhai H, Tian H, et al. Generation of Fully-Covering Hierarchical Micro-/nano- Structures by Nanoimprinting and Modified Laser Swelling. Small. 2014;10:2595–601.

[21] Liimatainen V, Sariola V, Zhou Q. Controlling Liquid Spreading Using Microfabricated Undercut Edges. Advanced Materials. 2013;25:2275-8.

[22] Tsai CG, Hsieh CM, Yeh JA. Self-alignment of microchips using surface tension and solid edge. Sensors and Actuators A: Physical. 2007;139:343-9.

[23] Fukushima T, Iwata E, Konno T, Bea JC, Lee KW, Tanaka T, et al. Surface tension-driven chip self-assembly with load-free hydrogen fluoride-assisted direct bonding at room temperature for three-dimensional integrated circuits. Applied Physics Letters. 2010;96:154105--3.

[24] Chang B, Shah A, Routa I, Lipsanen H, Zhou Q. Low-height sharp edged patterns for capillary self-alignment assisted hybrid microassembly. J Micro-Bio Robot. 2014:1-10.

[25] Hoo JH, Park KS, Baskaran R, Böhringer KF. Template-based self-assembly for silicon chips and 01005 surface-mount components. Journal of Micromechanics and Microengineering. 2014;24:045018.

[26] Shah A, Chang B, Suihkonen S, Zhou Q, Lipsanen H. Surface-Tension-Driven Self-Alignment of Microchips on Black-Silicon-Based Hybrid Template in Ambient Air. Journal of Microelectromechanical Systems. 2013;22:739-46.

[27] Routa I, Chang B, Shah A, Zhou Q. Surface Tension-Driven Self-Alignment of Microchips on Low-Precision Receptors. Journal of Microelectromechanical Systems. 2013;PP:819-28.

[28] Berthier J, Brakke K, Grossi F, Sanchez L, Di Cioccio L. Self-alignment of silicon chips on wafers: A capillary approach. Journal of Applied Physics. 2010;108:054905.

[29] Liimatainen V, Sariola V, Quan Z. Undercut edges for robust capillary self-alignment in hybrid microassembly. 8th IEEE International Conference on Nano/Micro Engineered and Molecular Systems (NEMS)2013. p. 1088-91.

[30] Gibbs JW. The scientific papers of J. Willard Gibbs: Longmans, Green and Company, 1906.

[31] Levy GN, Schindel R, Kruth JP. Rapid manufacturing and rapid tooling with layer manufacturing (LM) technologies, state of the art and future perspectives. CIRP Annals - Manufacturing Technology. 2003;52:589-609.

[32] Khajavi SH, Partanen J, Holmström J. Additive manufacturing in the spare parts supply chain. Computers in Industry. 2014;65:50-63.

[33] Bargiel S, Rabenorosoa K, Clévy C, Gorecki C, Lutz P. Towards micro-assembly of hybrid MOEMS components on a reconfigurable silicon free-space micro-optical bench. Journal of Micromechanics and Microengineering. 2010;20:045012.

[34] Clévy C, Lungu I, Rabenorosoa K, Lutz P. Positioning accuracy characterization of assembled microscale components for micro-optical benches. Assembly Automation. 2014;34:69-77.

[35] Claverley JD, Leach RK. A vibrating micro-scale CMM probe for measuring high aspect ratio structures. Microsystem Technologies. 2009;16:1507-12.

[36] Claverley J, Burisch A, Leach R, Raatz A. Semi-automated assembly of a MEMS-based micro-scale CMM probe and future optimization of the process chain with a view to desktop factory automation. Precision Assembly Technologies and Systems2012. p. 9-16.

[37] Stalder AF, Melchior T, Müller M, Sage D, Blu T, Unser M. Low-bond axisymmetric drop shape analysis for surface tension and contact angle measurements of sessile drops. Colloids and Surfaces A: Physicochemical and Engineering Aspects. 2010;364:72-81.

Table captions

Table 1: Table summarising the average actual edge geometry compared to the nominal value.

Table 2: Summary of self-assembly tests carried out. Edge geometry represents actual angle, with corresponding nominal angle shown in square brackets.

Figure captions

Figure 1: Self-alignment of component using liquid surface tension. a) Liquid droplet dispensed onto binding site and component moved into place, b) component comes into contact with liquid droplet and meniscus is formed, c) restoring forces act on component and it aligns to shape of binding site due to energy minimisation.

Figure 2: Diagram illustrating the quantities used in Young's equation (1).

Figure 3: Spreading of a liquid droplet meeting a sharp edge as described by the Gibbs inequality, equation (2).

Figure 4: a) Rendered image of test component with array of Ø0.5 mm circular binding sites, b) Rendered image of a single binding site with 45°nominal edge geometry, c) SEM image of Ø0.6 mm circular binding site with 60° nominal edge geometry.

Figure 5: Cross-sectional diagram of binding site geometry for Ø0.5 mm circular binding site.

Figure 6: Nominal edge geometries of topographical structures. Blue region indicates liquid droplet placed on top surface of the structure.

Figure 7: Optical microscope images of water droplets; a) unconstrained droplet on plain substrate, b) isometric view of droplet constrained to Ø1 mm circular binding site with 60° nominal edge geometry.

Figure 8: Contact angle of water droplets on circular binding sites for full range of nominal edge geometries. Error bars display standard deviation.

Figure 9: Contact angle of water droplets on circular binding sites for different nominal edge geometries. Error bars display standard deviation.

Figure 10: SEM images showing defects present on circular binding sites; a) and b) show Ø0.4 mm x 45° edge geometry, c) and d) show Ø0.6 mm x 45° edge geometry. White arrows indicate cracks in the structure caused by contraction due to evaporation in the curing process.

Figure 11: Contact angle of water droplets on square binding sites for different nominal edge geometries. Error bars display standard deviation.

Figure 12: Optical microscope images of cross-sectioned binding sites. a) 60° nominal, b) 90° nominal, c) 105° nominal, and d) 135° nominal.

Figure 13: Schematic showing the three assembly cases examined in this work. Dotted line represents release position for component: a) x-offset, b) twist-offset, and c) droplet misalignment.

Figure 14: Assembly results for x-offset tests: a) scatter plot and b) box plot. Dotted lines indicate threshold regions of 25and 100 μm misalignment in the x-axis. Numbers in square brackets represent the nominal edge geometries. Asterisks indicate outliers in the data.

Figure 15: Bar charts showing component assembly success rates for misalignments less than or equal to the given threshold in both x and y axis: a) x-offset, b) twist-offset, c) droplet misalignment. X-axis displays the measured edge geometry, with corresponding nominal angle shown in square brackets.

Figure 16: Boxplots of assembly results showing magnitude of component misalignment in both x and y axis against binding site edge geometry for assembly cases falling within the ±100 μm threshold: a) x-offset, b) twist-offset, c) droplet misalignment. Asterisks indicate outliers in the data.

Figure 17: SEM images of 2 x 2 mm assembly structures. a) 45° nominal edge geometry, b) 45° nominal with incorrectly manufactured edge geometry, c) top-down view of 105° structure, d) 135° structure clearly showing stepping of individual 25 μm layers.